ARTICLE

Recovery of Permittivity and Depth from Near-Field Data as a Step toward Optical Nanotomography

Alexander A. Govyadinov,[†,*] Stefan Mastel,[†] Federico Golmar,[†,‡] Andrey Chuvilin,[†,§] P. Scott Carney,[⊥] and Rainer Hillenbrand[§,∥,*]

[†]CIC Nanogune Consolider, 20018 Donostia-San Sebastián, Spain, [‡]I.N.T.I.-CONICET and ECyT-UNSAM, San Martín B1650JKA, Argentina, [§]IKERBASQUE, Basque Foundation for Science, 48011 Bilbao, Spain, [⊥]Department of Electrical and Computer Engineering and the Beckman Institute for Advanced Science and Technology, University of Illinois, Urbana, Illinois 61801, United States, and [∥]CIC nanogune consolider and UPV/EHU, 20018 Donostia-San Sebastián, Spain

ABSTRACT The increasing complexity of composite materials structured on the nanometer scale requires highly sensitive analytical tools for nanoscale chemical identification, ideally in three dimensions. While infrared near-field microscopy provides high chemical sensitivity and nanoscopic spatial resolution in two dimensions, the quantitative extraction of material properties of three-dimensionally structured samples has not been achieved yet. Here we introduce a method to perform rapid recovery of the thickness and permittivity of simple 3D structures, such as thin films and nanostructures from near-field measurements, and provide its first experimental demonstration. This is accomplished *via* a novel nonlinear invertible model of the imaging process, taking advantage of the near-field data recorded at multiple harmonics of the oscillation frequency of the near-field probe. Our work enables the quantitative nanoscale-resolved optical studies of thin films, coatings, and functionalization layers, as well as the structural analysis of multiphase materials, among others. It represents a major step toward the further goal of a general near-field tomography of samples.

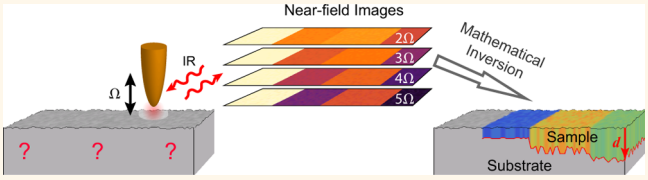

KEYWORDS: chemical imaging · nanotomography · inverse problems · near-field microscopy · thin films · s-SNOM · ellipsometry

Infrared (IR) radiation is highly sensitive to the molecular and electronic properties of matter and thus provides an excellent probe for noninvasive identification and characterization of thin samples. By performing IR spectroscopy, such as Fourier transform infrared spectroscopy (FTIR),[1] the chemical composition of materials can be identified. More quantitative details about the sample can be inferred by performing IR ellipsometry[2] that returns dielectric permittivity of the sample material as well as its structural properties, such as thickness for thin samples and films. However, these far-field techniques are limited by diffraction to the lateral resolution of about half the wavelength of light employed ($\lambda \sim 10\,\mu$m at mid-IR), which significantly restricts their application to nanoscience and nanotechnology where an examination of objects at 10−100 nm scale is desired.

Scattering-type scanning near-field optical microscopy (s-SNOM) is a powerful technique that provides wavelength-independent nanoscale resolution even at IR frequencies.[3] In s-SNOM, typically an atomic force microscope (AFM) tip is illuminated by an external IR source and the backscattered radiation is detected. The tip, usually a sharp metal-coated probe, concentrates IR light and creates a strong near-field tightly confined around the tip apex.[4,5] This near-field interacts with a small sample volume below the apex, with the interaction being manifested in the tip backscattering. Thus, s-SNOM images obtained by scanning the sample surface represent *two-dimensional* (2D) near-field maps of sample properties. Such near-field maps can be utilized for mapping the spatial distribution of constituents on the sample surface[6−12] with lateral resolution below 20 nm and a possibility of their further chemical identification using s-SNOM-based nanospectroscopy.[9,13−17]

Recently, s-SNOM has shown the ability for *quantitative* analysis of samples, such as the determination of their permittivity (dielectric function).[18−20] However, the

* Address correspondence to a.govyadinov@nanogune.eu, r.hillenbrand@nanogune.eu.

Received for review March 24, 2014 and accepted June 4, 2014.

Published online 10.1021/nn5016314

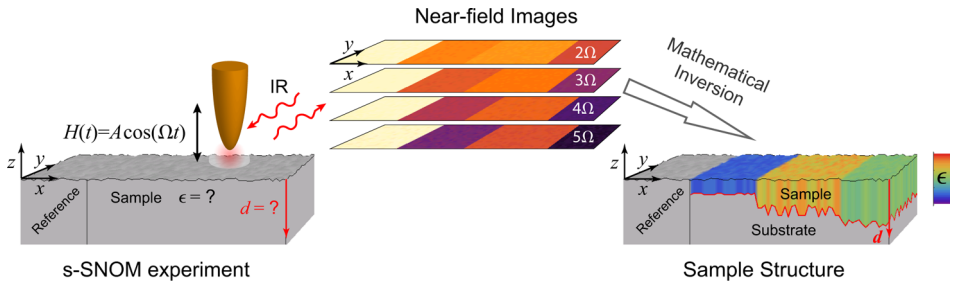

Figure 1. Schematics of the s-SNOM experiment and the conceptual representation of the reconstruction procedure that yields the sample structure. The scattered field originated by an externally illuminated oscillating AFM tip is detected interferometrically and demodulated at higher harmonics of the tip oscillation frequency. By scanning the sample surface, a set of near-field images is recorded and further normalized to the signal on a reference area with known optical properties. A mathematical inversion procedure is then applied to each pixel to recover the sample structure, *i.e.*, thickness (represented by red curve) and dielectric permittivity (represented by fill color) of the sample layer at each lateral position.

demonstrated derivations required a prior knowledge about vertical distribution of sample constituents below the surface. Indeed, the s-SNOM tip interacts with a three-dimensional (3D) volume that extends below the sample surface to depths of ~100 nm,[18,21] thus revealing the subsurface features in near-field maps. Despite the demonstrated ability of such subsurface detection,[22−24] the reconstruction of the 3D sample structure from near-field experiments (also referred to as near-field tomography) is a nontrivial task[25−29] and has not yet been demonstrated experimentally. One of the challenges is that a single s-SNOM image provides insufficient data for volumetric reconstruction as it represents a 2D map of interaction between the tip and the *three-dimensional* sample volume.[28,30−32] This presents a fundamental problem analogous to that of inferring the shape of a 3D object by its single 2D projection. Another challenge relates to the evanescent nature of near-fields involved in the tip−sample interaction, which makes an *inversion* (*i.e.*, the mathematical procedure that recovers sample properties from the near-field data) highly unstable in the presence of noise.[33] These challenging problems resulted in s-SNOM being traditionally regarded as a technique for surface studies.

In this work, we break the traditional view on s-SNOM by demonstrating that the in-depth sample structure (thickness and permittivity) can be *quantitatively* recovered solely from the near-field images (see the concept Figure 1). We show that the additional data necessary for subsurface studies can be obtained from near-field images recorded at *multiple harmonics* of the scattered signal. These harmonics are routinely obtained in s-SNOM as a result of the background suppression technique according to which the tip height is modulated at a frequency Ω of few hundred kHz and the detected signal is demodulated at higher harmonics of this frequency.[3,34,35] Different harmonics manifest different interaction volumes (see Figure 5a), thus probing different sample depths.[23,36] In contrast to other proposed approaches, such as sample rotation and volumetric scanning,[18,28,37] utilization of information contained in multiple harmonics of the detector signal is natural for s-SNOM and thus presents a simple, practical method of obtaining necessary information for subsurface studies.

To recover the volumetric information encoded in high harmonics of the detector signal, we developed a perturbative model that describes interaction of the s-SNOM tip with a film (regarded as a sample) deposited on a substrate. The key advantage of our model is that it allows for an analytic inversion of the associated scattering problem with respect to the sample permittivity, parametrized by a single depth/thickness variable. The correct film thickness is then obtained by enforcing the consistency of results derived from different harmonics of the scattered signal. Mathematically, this formulates a one-dimensional minimization problem, compared to three-dimensional minimization procedures required in possible brute-force approaches that seek to simulate the near-field scattering by varying three parameters: real and imaginary parts of sample permittivity and its thickness. Such substantial problem simplification significantly improves the speed and, importantly, the stability of the inversion.

RESULTS AND DISCUSSION

We begin by developing a general model of the scattering process that occurs when a s-SNOM tip is placed near a transversely homogeneous medium of permittivity ε. The total field E around the tip obeys the reduced wave equation:

$$\nabla \times \nabla \times \mathbf{E}(\mathbf{r}) - k_0^2(1 + 4\pi\chi_t(\mathbf{r}))\mathbf{E}(\mathbf{r}) = 4\pi k_0^2 \chi(\mathbf{r})\mathbf{E}(\mathbf{r}) \quad (1)$$

where $\chi = (\varepsilon - 1)/(4\pi)$ stands for the susceptibility of the medium below the tip, χ_t for that of the tip, and $k_0 = 2\pi/\lambda$ is the free-space wavenumber. Equation 1 can be cast into an integral form with the aid of Green tensors $\hat{G}(\mathbf{r},\mathbf{r}')$ and $\hat{G}_{tip}(\mathbf{r},\mathbf{r}') = \hat{G}(\mathbf{r},\mathbf{r}') + \int_{tip}\hat{G}(\mathbf{r},\mathbf{r}'')\chi_t(\mathbf{r}'')\hat{G}_{tip}(\mathbf{r}'',\mathbf{r}')d^3r''$, whose actions on an elementary source placed at position r' yields the field at any other position r that is produced by this source in free-space and in the

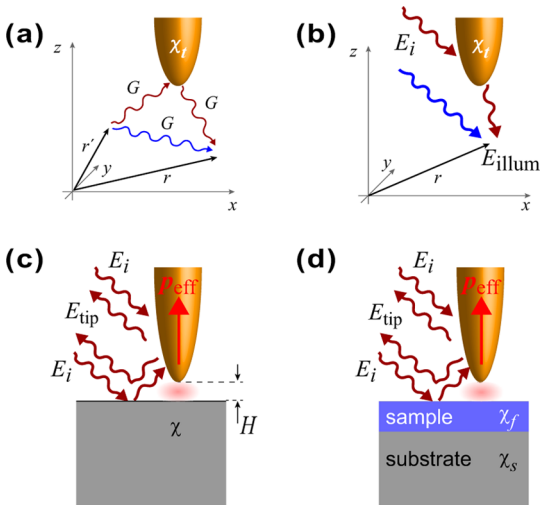

Figure 2. (a) Schematic representation of the Green function in the presence of the tip $G_{tip}(\mathbf{r},\mathbf{r}')$ that is contributed by two parts: the direct one (blue) and that through scattering by the tip (red). (b) Schematic representation of $\mathbf{E}_{illum}$ composed of the direct illumination $\mathbf{E}_i$ (blue) and that through the tip (red). (c) Illustration of s-SNOM scattering from an arbitrary sample of susceptibility χ. (d) Same as in (c), but with sample composed of a thin film.

F2 presence of the tip, respectively (see Figure 2a):

$$\mathbf{E}(\mathbf{r}) = \mathbf{E}_{illum}(\mathbf{r}) + \int d^3r' \hat{G}_{tip}(\mathbf{r},\mathbf{r}')\chi(\mathbf{r})\mathbf{E}(\mathbf{r}') \quad (2)$$

Here $\mathbf{E}_{illum}(\mathbf{r})$ is the field when $\chi = 0$, represented in Figure 2b, that illuminates the sample by direct incidence $\mathbf{E}_i$ (blue channel) and by the scattering from the tip (red channel). The integral in eq 2 is taken over the whole volume of material below the tip.

A formal solution to eq 2 can be obtained using Born series which, after appropriate term grouping, takes the following form:

$$\mathbf{E} = (\hat{I} + \hat{S})\mathbf{E}_i + \mathbf{E}_{tip} \quad (3)$$

$$\mathbf{E}_{tip} = (\hat{I} + \hat{S})\hat{T}_s(\hat{I} + \hat{S})\mathbf{E}_i \quad (4)$$

where $\hat{I}$ is the identity matrix and $\hat{T}_s$ is a matrix that describes the scattering by the tip, as well as all multiple scattering events between the tip and the sample:

$$\hat{T}_s = \hat{T} + \hat{T}\hat{S}\hat{T} + \hat{T}\hat{S}\hat{T}\hat{S}\hat{T} + \ldots \quad (5)$$

with $\hat{T}$ and $\hat{S}$ being the self-depolarizations[38] of the tip and the sample, respectively. We note that the incorporation of higher-order terms such as $\hat{T}\hat{S}\hat{T}$ in theoretical description of $\hat{T}_s$ is essential for the volumetric studies.[39]

The first term in eq 4 corresponds to the (strong) scattering by the whole illuminated part of the sample and is part of the background. The second term, $\mathbf{E}_{tip}$, contains the contribution from the near-field interaction between the tip and the nanoscopic volume of the sample below the tip apex, thus enclosing the *local* information about the sample. $\mathbf{E}_{tip}$ can be understood within quasistatic approximation by interpreting $\hat{S}$ as the far-field reflection coefficient r_s of the sample and $\hat{T}_s$ as the effective polarizability α_{eff} of the tip above it, yielding a familiar form for the vertical field component:

$$E_{tip} \propto (1 + r_s)\alpha_{eff}(1 + r_s)E_i \quad (6)$$

Equation 6 has a simple intuitive explanation depicted in Figure 2c. Namely, the tip illuminated directly and *via* scattering from the sample interacts with the sample *via* near-field. This results in the formation of a primarily vertical effective dipole $p_{eff} = \alpha_{eff}(1 + r_s)E_i$, which, in turn, radiates to the far-field directly and *via* the reflection from the sample.[3,40,41]

In experiment, E_{tip} has to be separated from the dominant background. This is achieved by providing a periodic modulation to the tip height $H = H(t) = A(1 + \cos(\Omega t))$ in time t with small amplitude $A \sim R_t \ll \lambda$ at a frequency Ω of a few hundred kHz (see Figure 1). The detector signal U_n is detected interferometrically and demodulated at harmonics $n\Omega$ of the tip oscillation frequency.[34,35] The background is largely insensitive to small variations in the tip height and therefore only contributes to lower harmonics. In contrast, the near-field interaction is highly nonlinear in tip−sample distance and dominates the detected signal at higher harmonics $n \geq 2$.[3,42] Note that $U_n = s_n \exp(i\phi_n)$ is complex-valued (here $s_n = |U_n|$), as the tip−sample interaction can introduce a phase $\phi_n = \arg(U_n)$ to the scattering that can be measured due to employed interferometric detection scheme.[3]

Considering only the harmonics for which the background is sufficiently suppressed, the U_n is determined by E_{tip} and is proportional to its nth Fourier coefficient with respect to time. (Note that E is still represented in the frequency domain, *i.e.*, $E = E(\omega)$ as implied by its prior definition. Due to the vertical tip oscillation, it also acquires the time dependence, $E = E(\omega,t)$. Such a mixing of frequency and time domains is possible because the tip oscillation is 9 orders of magnitude slower compared to the IR frequency and the tip can thus be regarded stationary at any moment of time.)

$$U_n \propto E_n = \hat{F}_n[E_{tip}(H(t))] = \int E_{tip}(H(t))e^{in\Omega t}dt \quad (7)$$

Since the coefficient of this proportionality is typically unknown, the measured signal U_n is normalized to that on a well-known reference. This procedure yields the (complex-valued) *near-field* contrast η_n

$$s_n/s_{n,ref}e^{i(\phi_n - \phi_{n,ref})} = \eta_n = E_n/E_{n,ref} \quad (8)$$

and also puts the phase measurements into prospective; that is, η_n measures the scattering phase relative to that on reference.

At fixed amplitude A, demodulation order n, tip material/composition, and reference material, η_n is determined by the dielectric properties of the sample and can be employed for the analysis of s-SNOM

measurements. Equation 8 serves as a base for such analysis as it draws the connection between experimentally measured near-field contrast (left-hand side) and the theory that describes near-field interaction between the tip and the sample (right-hand side). By modeling this interaction, one can simulate the measured near-field contrast and even extract the dielectric properties of the sample from it. The latter can be achieved by variation of sample permittivity and thickness until the simulated contrast matches that of the experiment,[15,18,20] or by direct mathematical *inversion* procedure.[19,43] The mathematical inversion seeks to describe near-field scattering through a scattering operator $\hat{A}$ that yields the contrast $\eta_n = \hat{A}(\varepsilon)$ and can be inverted; that is, the sample permittivity can be found as $\varepsilon = \hat{A}^{-1}(\eta_n)$. Such approach can dramatically reduce the computational complexity and often improves the stability of the problem.[27,44] The improved stability is especially useful here since near-field scattering deals with exponentially decaying fields, thus yielding growing exponential in the inverse of $\hat{A}$ that can quickly amplify any experimental noise and render the extraction of sample parameters unfeasible.[33]

Up to now, the developed formalism has been very general and applies to arbitrary samples. We now adapt it to thin-film samples for which $\chi(r)$ can be decomposed into two transversely homogeneous parts: susceptibility of the film χ_f (also referred to as sample) and that of the substrate χ_s (see Figure 2d). Assuming without the loss of generality that the film occupies a region $-d_0 \le z \le 0$, we split the integral along the z-direction in the right-hand side of eq 2 into three parts: $\int_{-\infty}^{-d_0} dz' \hat{G}_{tip} \chi \mathbf{E} = \chi_s \int_{-\infty}^{-d_0} dz' \hat{G}_{tip} \mathbf{E} + \chi_f \int_{-\infty}^{0} dz' \hat{G}_{tip} \mathbf{E} - \chi_f \int_{-\infty}^{-d_0} dz' \hat{G}_{tip} \mathbf{E}$. Each part corresponds to the scattering by a virtual semi-infinite half-space occupied by either the material of susceptibility χ_s or χ_f and beginning at $z = 0$ or $z = -d_0$. The Born series expansion of eq 2 now results in $\hat{T}_s$ being represented as

$$\hat{T}_s = \hat{T}_s(\chi_s, d_0) + \hat{T}_s(\chi_f, 0) - \hat{T}_s(\chi_f, d_0) + 2\hat{T}_s(\chi_f, d_0)\hat{T}_s(\chi_f, d_0) + \mathrm{HO} \quad (9)$$

where each of the first three terms $\hat{T}_s(\chi,d)$ corresponds to the tip interacting with a single virtual half-space of susceptibility χ beginning at $z = -d$ and resembling the structure of eq 5. They can be regarded as the first order of a generalized interaction series and are schematically represented in Figure 3 which provides an intuitive interpretation.

The fourth term in eq 9 is part of the higher-order corrections (HO) that correspond to multiple interactions between the tip and virtual half-spaces mediated by the tip. Here we limit ourselves to the second-order interactions which, apart from the aforementioned fourth term in eq 9, can be represented as permutations of three elements $\hat{T}_s(\chi_s,d_0)$, $\hat{T}_s(\chi_f,0)$, and $-\hat{T}_s(\chi_f,d_0)$

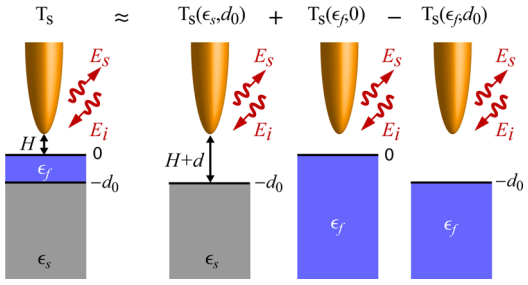

Figure 3. Schematic representation of the first-order terms in eq 9.

containing two nonidentical elements. Higher expansion orders can be considered depending on the desired approximation accuracy.

The advantage of the developed approach is that it reduces the near-field scattering from a thin film to that produced by a number of virtual semi-infinite half-spaces (*i.e.*, bulks). This enables the development of an efficient inversion routine based on a variety of currently developed models that describe near-field scattering in tip−bulk systems. Here, we adopt a traditional finite dipole model (FDM)[40] that treats the tip as a conductive spheroid and models its interaction with a semi-infinite (bulk) medium within quasistatic approximation. Compared to other models,[3,18,20] the FDM provides a good compromise between the accuracy and the modeling complexity.[19] Within the FDM, operators $\hat{T}_s(\chi,d)$ in eq 9 reduce to the "bulk" effective polarizabilities $\alpha_{blk}(\varepsilon,d)$ that describe the near-field scattering from the tip placed above a semi-infinite half-space of permittivity ε that is offset by distance d down from the origin determined by the film−air interface (see Figure 3):

$$\alpha_{blk}(\varepsilon, d) = C(2 + \xi(\beta, d)) \quad (10)$$

where ξ stands either for $\xi_0 = f_0(H + d)\beta(\varepsilon)[1 - f(H + d)\beta(\varepsilon)]^{-1}$ or for $\xi_1 = f(H + d)\beta(\varepsilon)[1 - f(H + d)\beta(\varepsilon)]^{-1}$ depending on the position of $\hat{T}_s$, and β is the quasistatic reflection coefficient that depends only on the permittivity ε:

$$\beta = \frac{\varepsilon - 1}{\varepsilon + 1} \quad (11)$$

Here f_0 and f are two functions that depend on the tip height above the sample surface, but not on ε (the expressions for f, f_0, and constant C are given in the Methods). The resulting effective polarizability of the tip above the film−substrate system (up to the second interaction order) can be expressed as

$$\begin{aligned}\alpha_{eff} \propto 2 &+ \xi_0(\varepsilon_s, d_0) + \xi_0(\varepsilon_f, 0) - \xi_0(\varepsilon_f, d_0) \\ &+ 2\xi_1(\varepsilon_f, d)\xi_0(\varepsilon_f, d) \\ &- (\xi_1(\varepsilon_f, 0)\xi_0(\varepsilon_f, d) + \xi_1(\varepsilon_f, d)\xi_0(\varepsilon_f, 0)) \\ &+ (\xi_1(\varepsilon_f, 0)\xi_0(\varepsilon_s, d) + \xi_1(\varepsilon_s, d)\xi_0(\varepsilon_f, 0)) \\ &- (\xi_1(\varepsilon_f, d)\xi_0(\varepsilon_s, d) + \xi_1(\varepsilon_s, d)\xi_0(\varepsilon_f, d))\end{aligned} \quad (12)$$

For samples composed of weak molecular oscillators, such as polymers, biological matter, and other materials for which the quasistatic reflection coefficient β does not significantly exceed unity, the α_{eff} can be expanded into a Taylor series in powers of β_f yielding[19]

$$\alpha_{eff} = \sum_{j=0}^{\infty} \alpha_j \beta_f^j \tag{13}$$

where β_f is the quasistatic reflection from bulk of permittivity ε_f and α_j is the expansion coefficients which are *independent* from ε_f. By substituting eq 13 into eq 6, performing the Fourier transform (7) and normalizing to the reference according to eq 8, we obtain the near-field contrast:

$$\eta_n = \frac{(1+r_s)^2}{(1+r_{s,ref})^2} \sum_{j=0}^{\infty} \beta_f^j \frac{\hat{F}_n[\alpha_j]}{\hat{F}_n[\alpha_{eff,ref}]} \tag{14}$$

The benefits of the perturbative scattering approach expressed by eq 9 and of the Taylor expansion of effective polarizability (13) can now be clearly seen, as eq 14 allows for a straightforward inversion. Indeed, truncated at a particular order J, it represents a simple polynomial equation for β_f. The near-field contrast η_n can be measured, while the coefficients in front of β_f^j in the sum are independent from the film permittivity and can be computed. The prefactor $R = (1 + r_s)^2/(1 + r_{s,ref})^2$ for optically thin films ($d_0 \ll \lambda$) discussed here is close to unity and will be neglected in the following.[19] Thus, eq 14 can be readily solved yielding β_f, from which the permittivity ε_f can be recovered *via* eq 11. The accuracy of such inversion can be controlled by the expansion order J. The neglected reflection can be accounted for through a perturbative procedure described in the Supporting Information of Govyadinov *et al.*[19]

The inversion procedure based on eq 14 is simple and robust and does not require models for the dielectric permittivity of the film.[19] However, it requires the knowledge of the film thickness d_0 to calculate expansion coefficients $\alpha_j = \alpha_j(d_0)$. If the film thickness is unavailable, it must be determined from the s-SNOM data; that is, at each imaged pixel, three values, namely, Re(ε), Im(ε), and film thickness d_0, have to be found. Measurements of the near-field contrast at a single harmonic provide only two values per pixel: magnitude $|\eta_n|$ and its phase arg(η_n). This prevents finding a unique solution to the inverse problem as different combinations of dielectric function and film thickness can result in the same near-field contrast at a single selected harmonic. Such an inverse problem is underdetermined and requires additional *independent* data in order to obtain a (unique) solution.

The key point of our work is that the required data can be obtained by considering several harmonics of η_n. It has been shown that the sensitivity of different harmonics to the subsurface composition of the sample varies with the harmonic number n: as n increases, the harmonic senses less and less into the depth of the sample.[18,23] Therefore, the film thickness is encoded in the relation between near-field contrasts with different n.

We thus propose the following simple procedure to determine the film thickness from the measurements. One utilizes eq 14 to compute film permittivities from a pair of near-field contrasts η_{n_1} and η_{n_2} (n_1 and n_2 can be any harmonic numbers that yield background-free signal) parametrized by a thicknesses parameter d. This procedure yields $\varepsilon_{n_1}(d)$ and $\varepsilon_{n_2}(d)$. In an ideal experiment, the difference $\varepsilon_{n_1}(d) - \varepsilon_{n_2}(d)$ is zero when evaluated at d corresponding to the correct film thickness d_0. In practice, d_0 can be found by minimizing the discrepancy between permittivities derived from different harmonics (*i.e.*, L_1 norm) with respect to d, or more reliably (taking the difference relative to the corresponding permittivity prevents the collapse of the solution toward small ε):

$$L_1 = \left| \frac{\varepsilon_{n_1}(d) - \varepsilon_{n_2}(d)}{\varepsilon_{n_1}(d) + \varepsilon_{n_2}(d)} \right| \tag{15}$$

The permittivity can then be found by evaluating $\varepsilon_n(d)$ at the value that minimizes L_1.

We emphasize that the minimization is only performed with respect to the film thickness and not to the unknown dielectric permittivity ε of film. The latter is obtained from the polynomial eq 14 and can be found analytically. This significantly reduces the dimensionality of the posed problem from three to one and improves the stability of the derivation procedure in the presence of noise.

Simulated Inversion. To illustrate the inversion procedure, let us recover the permittivity of a hypothetical sample from the simulated near-field data. For this purpose, we assume that the sample comprises a poly(methyl methacrylate) (PMMA) film of thickness $d_0 = 20$ nm and permittivity $\varepsilon_f = 1.67 + 0.97i$ deposited onto silicon substrate of permittivity $\varepsilon_{Si} = 11.7$ (Figure 4a). F4 We further assume that the simulated contrasts η_3, η_4, and η_5 are available for the inversion. To simulate these η_n, we calculate the effective polarizability according to eq 12 and its Fourier coefficients according to eq 7. This yields E_n at the sample location. The reference $E_{n,ref}$ is assumed to be the film substrate and is calculated using the bulk polarizability model (10). The normalization according to eq 8 yields the desired near-field contrasts. The employed simulation parameters are A = 60 nm, R_t = 20 nm, L = 600 nm, $g = 0.7\exp(i0.06)$ (see Methods for the description of FDM model parameters).

We now compute $\varepsilon(d)$ as a function of depth parameter d by inverting (solving) eq 14 for each of the available η_n (using the same FDM model parameter as before and the expansion order J = 7 in eq 14). As can be seen from Figure 4b,c, all three computed

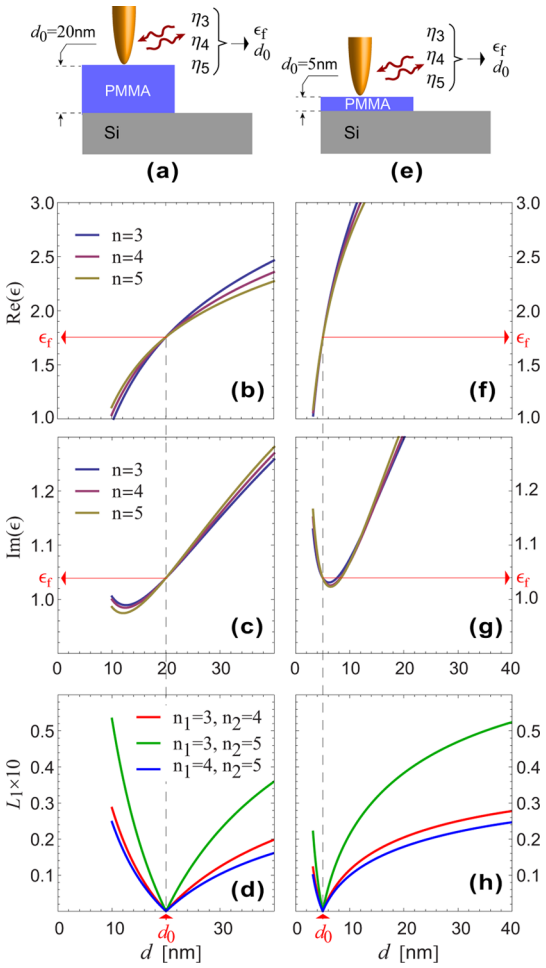

Figure 4. Schematics of the simulated inversion for PMMA films of 20 nm (a–d) and 5 nm thickness (e–h). (b,f) Real part of film permittivity as a function of depth parameter d determined by inversion from near-field contrasts obtained at harmonics n = 3,4,5. (c,g) Same for the Im(ε). (d,h) L_1 as a function of d plotted for various pairs of harmonics. Note that its minimum corresponds to the correct thickness d_0 (marked by dashed gray lines) of the PMMA film at which the permittivities derived from different harmonics coincide and yield the correct value ε_f (marked by red arrows).

curves intersect at the same value of depth d = 20 nm; that is, the differences between values of ε derived from different harmonics L_1 (depicted in Figure 4d) is zero for the depth that matches the correct film thickness. This proves that the minima of L_1 can be used to determine d_0. The value of the film permittivity can be subsequently recovered by evaluating $\varepsilon(d = d_0)$ (red arrows in Figure 4b,c).

Interestingly, the width of the dip around d_0 in L_1 tends to decrease with the film thickness as demonstrated by the simulation with a 5 nm thick film in Figure 4e–h. The narrow dips can be easily missed or yield inconsistent results across different harmonics in the presence of unavoidable experimental noise. This obscures the minimization procedure and limits the smallest film thicknesses that can be recovered by inversion depending on the quality of experimental data. At the same time, $\varepsilon(d)$ exhibits a larger variance under the small changes of depth parameter around d_0 for thinner films (see Figure 4b,c,f,g). This decreases the stability of the inversion and increases the uncertainty in the recovered permittivity for ultrathin films.

Note that, in principle, near-field measurements at only two harmonics are necessary for the recovery of the film depth along with its permittivity. However, the experimental noise can result in multiple local minima of L_1 and/or variation of the minimum position depending on the pairs of harmonics. Additional harmonics can help in determination of the correct film thickness by selecting the one that minimizes L_1 for *all* pairs, thus improving the reliability of the minimization procedure.

Determination of SiO_2 Thickness from Experimental Data. To check the feasibility of the inversion with experimental data, we performed s-SNOM measurements on a SiO_2 film. The film forms a wedge of gradually increasing thickness (see Figure 5a), which was obtained by mechanical polishing at a shallow angle of ~2° of a commercial Si wafer covered with a 300 nm layer of thermally grown oxide. F5

The SiO_2 wedge was imaged with a standard commercial s-SNOM (NeaSNOM, neaspec.com) in which an ordinary Au-coated AFM tip (apex radius $R_t \approx 20$ nm) was illuminated by a quantum cascade laser (TLS-21060, Daylight Solutions) at λ = 1732 cm^{-1}. Typical imaging parameters Ω = 138 kHz, $A \approx 50$ nm, and 20 ms integration time per pixel were employed. Figure 5b shows the magnitude of near-field contrasts at n = 3,4,5 obtained by normalizing U_n measured along the wedge to their average values at the exposed silicon (area of the strong signal around unity on the left). As SiO_2 is almost nonabsorbing at the selected wavelength, the phase arg(η_n) was neglected. The contrasts slowly decrease as the strongly reflective Si vanishes below the increasing layer of SiO_2, suggesting the variation of the oxide thickness but not directly revealing its thickness.

In order to determine the wedge thickness profile, we have performed the inversion of the near-field data according to eq 14. Three pairs of harmonics were utilized (n_1,n_2) = (3,4), (3,5), and (4,5). For the inversion, we have used L = 600 nm and g = 0.7 exp(i0.06) in the FDM[14] and went up to J = 11 in the Taylor expansion of α_{eff}. (The value of J for which the expansion converges depends on the film thickness.) The reference silicon was assumed to have permittivity ε_{Si} = 11.7.[45]

Figure 5c shows the recovered thickness profiles of the wedge d_{n_1,n_2} obtained by minimization of L_1 for the corresponding pairs of harmonics. The black line shows the thickness obtained by averaging of all d_{n_1,n_2}. The recovered profiles match well with the inclination of the Si–SiO_2 interface obtained from the scanning transmission electron microscope (STEM) image of the wedge cross section (gray line in Figure 5c).

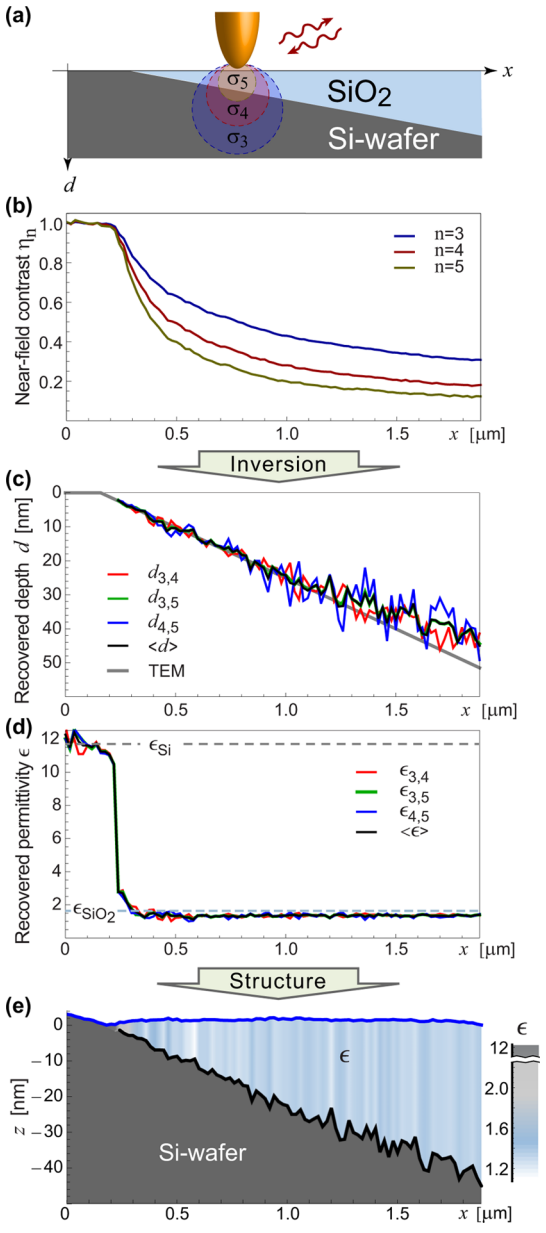

Figure 5. (a) Schematics of the SiO_2 wedge. Circles emanating from the tip represent the probing volumes for different harmonics. (b) Absolute value of near-field contrasts measured by s-SNOM at harmonics n = 3,4,5 as a function of position along the wedge. (c) Recovered thickness d_{n_1,n_2} of SiO_2 film as a function of lateral position obtained from various pairs of harmonics n_1 and n_2; black curve is the average yielded by all pairs. The gray line shows the estimate for the wedge profile derived from STEM image (not shown). (d) Recovered film permittivity. Each ε_{n_1,n_2} curve represents the mean of permittivities $\varepsilon(d_{n_1,n_2})$ derived by inversion from η_{n_1} and η_{n_2}; black curve represents their average. Horizontal dashed lines mark the permittivities of Si and SiO_2. (e) Depth profile of the wedge (solid black) obtained by subtraction of recovered film thickness from the sample topography returned by AFM (blue). The fill color represents the value of dielectric permittivity.

With the SiO_2 film thickness successfully recovered, we evaluate the permittivity of the oxide for each point along the wedge. The results obtained by averaging pairs of permittivities $\varepsilon(d_{n_1,n_2})$ obtained from η_{n_1} and η_{n_2} are plotted in Figure 5c. As one would expect, the derived permittivity stays constant on oxide, with its value closely matching that produced by the three-term Sellmeier equation for SiO_2[46] despite the changing film thickness. At Si ($x \lesssim 200$ nm), the film depth becomes undefined, as the minimization procedure tries to recover the thickness of the film made of the same material as the substrate below it. Since one can place a virtual interface anywhere between two identical materials, such procedure can yield an arbitrary value of d_0 that we do not show here, however, it returns the correct value of its permittivity (see Figure 5c). In our case, we have successfully recovered the permittivity of Si. The increased variance of the result is due to lower stability of the inversion for thin films, as we described in the previous section. In combination with the experimental noise, such instability can cause the failure of minimization. In our case, the thickness recovery starts failing for depths smaller than 2 nm and is not presented in Figure 5. The recovered permittivity in the region $2 < d_0 < 5$ nm varies from its value on SiO_2 to that on Si. This can be attributed to the assumption in the employed model that the film below the tip is homogeneous and has constant thickness. The latter, however, changes gradually, causing the minimization to output the thickness averaged over a lateral distance $x \sim 2R_t$. For our wedge, this can cause the mis-estimate the depth by about 1 nm. While this value can be safely ignored most of the time, it becomes relatively large for thin films and results in observed recovery of some averaged value of permittivity between the film and the substrate.

Figure 5b shows the recovered thickness of the oxide film assuming the sample is flat. Our sample, however, has a slightly varying topography, as returned by the AFM (top blue line in Figure 5d). To better visualize the in-depth profile of such sample, we subtract the average recovered film thickness from the topography, yielding the location of the Si−SiO_2 within the sample (black line in Figure 5d). The fill color represents the average value of the recovered local permittivity of the film.

Inversion for Nanostructured Samples. While the inversion of the near-field data measured on the SiO_2 wedge demonstrates the practical feasibility of the procedure, it does not contain lateral variation of the sample structure at nanoscale. In order to elucidate the lateral resolution limits of the presented model, we perform s-SNOM measurements of a sample composed of PMMA squares of varying sizes. To manufacture this sample, the PMMA was spin-coated onto the standard Si substrate to form a film of 40 nm thickness. The areas of varying sizes were then patterned with electron beam lithography (EBL) followed by the standard lift-off procedure (see Methods). The result of fabrication is a patterned sample with a set of PMMA squares of different lateral sizes located on the Si substrate.

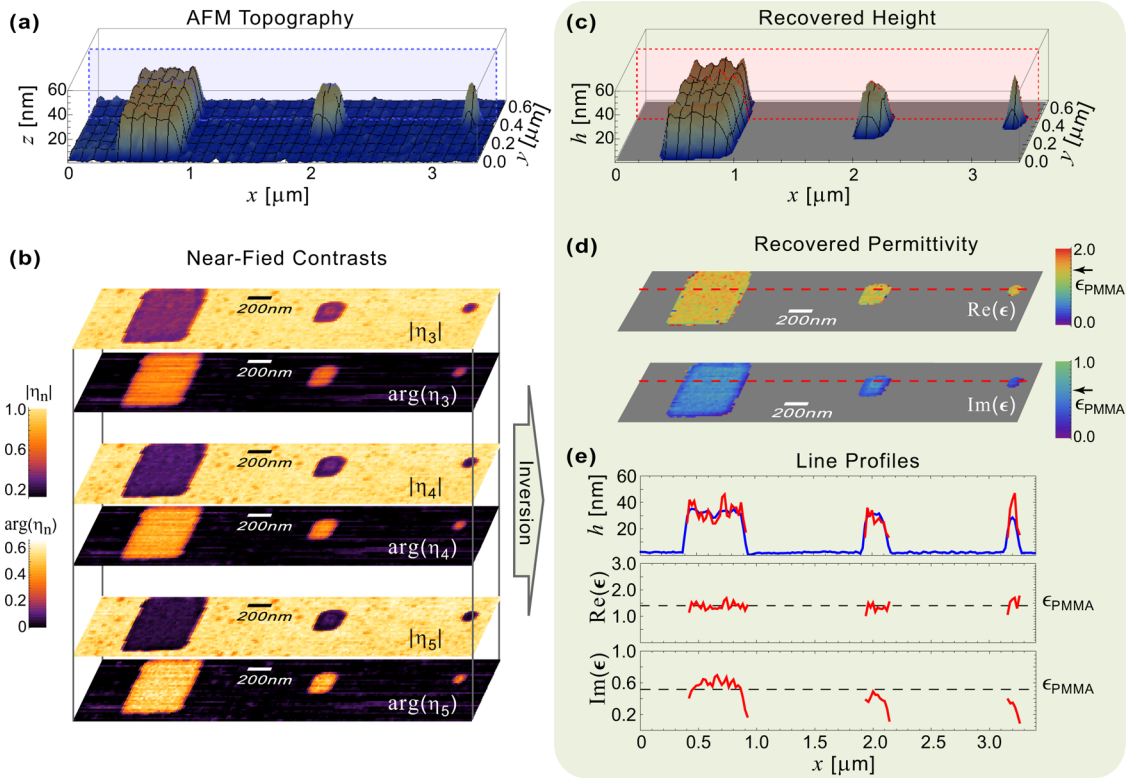

Figure 6. (a) Three-dimensional rendering of the sample topography measured by AFM. (b) Two-dimensional maps of absolute value and the phase of complex-valued near-field contrasts at $n = 3,4,5$ used for the inversion. The color scales are the same for all harmonics. (c) Averaged sample height d_0 recovered from the near-field measurements presented in panel b. Only the data on PMMA are shown, as the thickness recovery on the exposed Si is unreliable due to high noise level and the presence of small PMMA particles (remainder of the incomplete lift-off) with sizes below the limits that can be treated with our theoretical model. Nearest-neighbor smoothing is applied. (d) Permittivity maps of the PMMA squares obtained by inversion. The arrow next to the color scales marks the permittivity of PMMA obtained by far-field ellipsometry. (e) Top: recovered height profile (red) overlaid with the sample topography (blue) taken along the dashed lines in panels a and c. Middle and bottom: extracted real and imaginary parts, respectively, of the sample permittivities taken along the dashed lines in panel d. Dashed horizontal line marks the known permittivity of PMMA.

This sample was imaged with s-SNOM at $\lambda = 1743\ \mathrm{cm}^{-1}$ with lateral resolution of 20 nm per pixel using a Au tip with the apex radius $R_t \approx 20$ nm and oscillation amplitude $A \approx 100$ nm. Such imaging yields 2D maps of near-field contrasts presented in Figure 6b. The area of exposed silicon between the first and the middle square was used as a reference for normalization. Each line profile was normalized separately to its average value on Si, taking care to avoid the PMMA residue (small dark spots in Figure 6b).

Three PMMA squares with dimensions of $500 \times 500\ \mathrm{nm}^2$, $200 \times 200\ \mathrm{nm}^2$, and $80 \times 80\ \mathrm{nm}^2$ can be identified from the near-field images by the lower magnitude of η_n compared to that on Si. Strong phase contrast relates to the absorption of PMMA at the selected wavelength.[9,16] While η_n is seen to vary with harmonic n,[23] the sample height cannot be immediately inferred from the images.

In order to obtain sample height h and permittivity ε, we invert the near-field data using our model. Figure 6c shows the recovered height of the PMMA squares (smoothed by nearest-neighbor averaging), which matches well the sample topography measured by AFM (Figure 6a). With sample thickness determined, we recover the permittivity of PMMA. Figure 6d maps the sample permittivity as a function of lateral position, which is in great correspondence with the known value of the dielectric permittivity for PMMA at the operating wavelength (marked by the arrow next to the color scale). The latter is courtesy of Röseler and the same as used previously in Hauer *et al.*,[18] Govyadinov *et al.*,[19] and Taubner *et al.*[47]

The recovered height and permittivity are less accurate in the proximity of PMMA boundaries, where the near-field interaction is weakened as the tip near-field extends outside of PMMA into the air, yielding the pronounced dark rims in near-field contrasts visible in Figure 6b. In such case, the film can no longer be considered as laterally homogeneous, thus violating the assumptions of the employed model. This limits the lateral resolution of our technique. As one can see from Figure 6e that presents nonsmoothed profiles of h and ε as a function of position x, the recovery succeeds about 40−60 nm into PMMA squares. This demonstrates the resolution of $\Delta x \sim 2-3R_t$, which is consistent with previous estimates.[19] As a consequence of

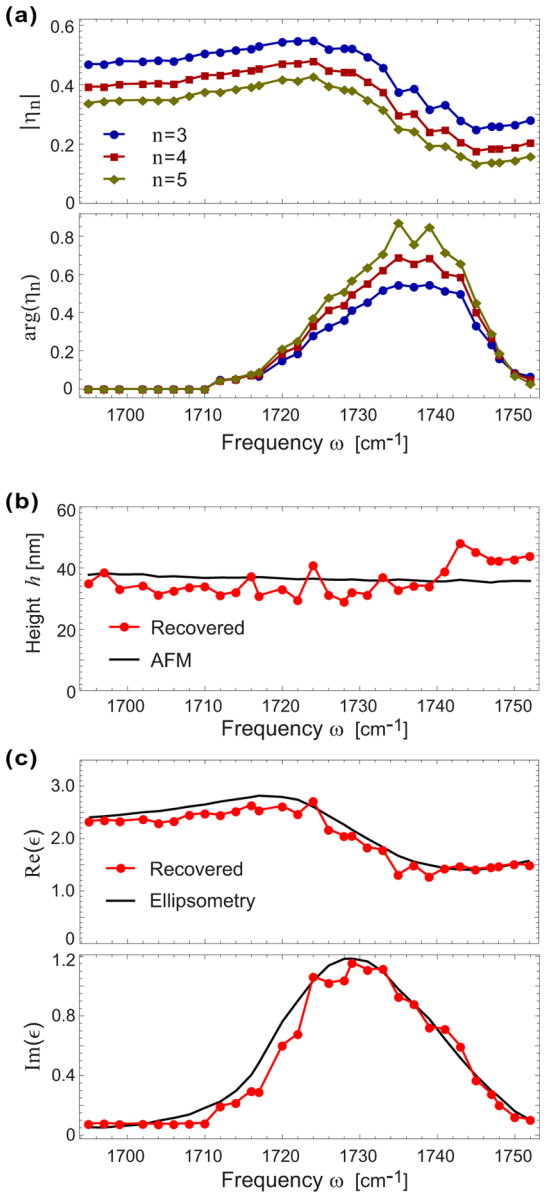

Figure 7. Averaged spectra of absolute value and phase of measured near-field contrasts (small phase for $\omega < 1712\ cm^{-1}$ is neglected) taken on the largest PMMA square depicted in Figure 6. (b) Averaged recovered height of the PMMA square as a function of wavelength (red). Solid black line shows the averaged height as determined by AFM topography. (c) Recovered spectra of sample permittivity (red). Solid black curves show the permittivity of PMMA obtained by far-field IR ellipsometry, courtesy of Prof. Röseler.

finite lateral resolution, the recovery procedure misestimates the height and the permittivity of the smallest nanostructure. Note, however, that the lateral resolution shown here is in no case a fundamental limit. It depends on the tip radius, oscillation amplitude, demodulation harmonic, *etc.*, leaving a lot of room for future studies and optimization.

Spectroscopic Reconstructions. To explore the prospects of performing spectroscopic reconstruction of dielectric permittivity of nanostructures from s-SNOM measurements, we have imaged the largest PMMA square at various wavelengths. This was achieved by tuning the laser in steps of $\approx 3\ cm^{-1}$. The tapping amplitude was set to $A \approx 60$ nm. By normalizing each line in the images to its average value at the exposed Si, we obtained the maps of near-field contrast. The spectrum of an average $\eta_n(\omega)$ at n = 3,4,5, taken over the area of $\sim 220 \times 220\ nm^2$ around the center of the PMMA square, is shown in Figure 7a. The selected spectral range encloses a pronounced resonance of PMMA corresponding to C═O stretching.[9] A small phase for frequencies $\omega < 1712\ cm^{-1}$ was ignored due to relatively high noise in measurements of phase contrast when the sample is weakly absorbing.

We inverted the obtained near-field data (assuming $R_t = 30$ nm, $A = 60$ nm, $L = 600$ nm, and $g = 0.7\exp(i0.06)$ for the FDM model) and determined the thickness and permittivity (averaged over results yielded by different harmonics) for each pixel in the middle of the square. The recovered values were then averaged and plotted in Figure 7b,c. As can be seen, the results of inversion are in great agreement with the average height derived from the AFM topography and spectra of permittivity obtained by far-field ellipsometry. This demonstrates the consistency of the results (obtained with the same model parameters) across multiple frequencies.

We note that the inversion based on the model developed for thick films[19] yields permittivity up to a factor of 2 larger than that of PMMA (data not shown), as that model is inappropriate for films thinner than ~100 nm.

CONCLUSIONS

In this work, we demonstrated that in-depth information about samples with deeply subwavelenth resolution in all three dimensions can be determined from experimentally obtained near-field data. To this end, we have successfully recovered from typical s-SNOM images the thickness and dielectric permittivity of a thin SiO_2 film of varying depth profile and several PMMA nanostructures of different lateral sizes.

Our work proves that multiple harmonics of the demodulated detector signal contain independent information sufficient for the recovery of sample subsurface composition and lays the theoretical foundation for its quantitative analysis. While formulated for a thin film on a simple substrate, our theory is not bound to a specific tip−bulk interaction model and can be extended to multilayered samples in a straightforward fashion.

Note that, owing to the quick and robust semianalytical inversion procedure, the recovery did not require line averaging or noise filtering and took less than 1 s per pixel (as implemented in Wolfram Mathematica on a personal workstation) for the target accuracy in thickness determination of 1 nm. Such performance

shows the practicality of real-time processing of near-field data.

Not yet being full near-field optical tomography, which is envisioned to reconstruct the arbitrarily shaped inhomogeneities within sample interior,[27] our work represents an important step for near-field techniques. It already enables the quantitative depth profiling of flat samples or samples in which optical/chemical properties do not necessarily correlate with the surface topography returned by AFM. Thus, our technique turns s-SNOM into a unique practical tool for noninvasive spectroscopic analysis of thin films or other heterogeneous samples with more than an order of magnitude better spatial resolution than available through far-field FTIR spectrometry and IR ellipsometry.

We note that as a general limitation of all near-field techniques, the sensitivity and resolution in s-SNOM degrades with depth. This places a practical limit on the thickness of the layer that can be tomographically reconstructed. The value of this thickness depends on the tip radius and imaging parameters but is typically confined to about 100 nm. Nevertheless, we imagine a great impact of our technique for investigation of multiphase materials, nanoscale-resolved studies of phase transitions, oxidation, and chemical processes, quality control of semiconductor devices, *etc*. with a broad scope of applications in chemistry, materials and biosciences, semiconductor industry, and other areas requiring quantitative measurements of thin subsurface layers with nanoscale spatial resolution.

METHODS

Preparation of Structured PMMA Sample by EBL. The PMMA squares were fabricated by high-resolution e-beam lithography. A layer of poly(methyl methacrylate) 950 kDa spin-coated onto a standard Si wafer was used as an electron-sensitive polymer. The unmasked area was exposed to a 120 μC/cm^2 dose, which is sufficient to completely develop the resist. The sample was then developed in methyl isobutyl ketone and isopropyl alcohol (IPA) at a ratio of 1:3. Finally, it was cleaned with IPA.

Brief Description of FDM. The tip height H in FDM[20] enters into the effective polarizability α_{blk} through two functions:

$$f_0(H) = \left(g - \frac{2H + W_0 + R_t}{2L}\right) \frac{\ln \dfrac{4L}{4H + 2W_0 + R_t}}{\ln \dfrac{4L}{R_t}} \qquad (16)$$

$$f(H) = \left(g - \frac{2H + W_i + R_t}{2L}\right) \frac{\ln \dfrac{4L}{4H + 2R_t}}{\ln \dfrac{4L}{R_t}} \qquad (17)$$

where $W_0 \approx 1.31R_tL/(L + 2R_t)$ and $W_i \approx R_t/2$ with R_t being the tip radius. The two model parameters, L = 600 nm and g = 0.7 exp(0.06i), represent the effective tip length and the fraction of induced charge participating in near-field interaction with the sample, respectively. They are obtained by fitting to the numerous experimental data and are practically invariant for all standard commercially available AFM tips.[14,40]

The constant $C \propto W_0^2 E_i$, which enters eq 10, determines the amount of total charge induced in the tip under external illumination in the absence of the sample.

Conflict of Interest: The authors declare the following competing financial interest(s): R.H. is a co-founder of Neaspec GmbH, a company producing scattering-type scanning near-field optical microscope systems, such as the one used in this study. All other authors declare no competing financial interests.

Acknowledgment. We thank C. Tollan for the preparation of the SiO_2 sample. We are also grateful to F. Huth for fruitful discussions on the subject. This research was funded by ERC Starting Grant No. 258461 (TERATOMO).

REFERENCES AND NOTES

1. Griffiths, P. R.; de Haseth, J. A. *Fourier Transform Infrared Spectrometry*; Wiley: New York, 2007.
2. Roeseler, A. *Infrared Spectroscopic Ellipsometry*; Akademie-Verlag: Berlin, 1990.
3. Keilmann, F.; Hillenbrand, R. In *Nano-Optics and Near-Field Optical Microscopy*; Richards, D., Zayats, A., Eds.; Artech House: Boston/London, 2009.
4. Huber, A. J.; Keilmann, F.; Wittborn, J.; Aizpurua, J.; Hillenbrand, R. Terahertz Near-Field Nanoscopy of Mobile Carriers in Single Semiconductor Nanodevices. *Nano Lett.* **2008**, *8*, 3766–3770.
5. Esteban, R.; Vogelgesang, R.; Kern, K. Full Simulations of the Apertureless Scanning Near Field Optical Microscopy Signal: Achievable Resolution and Contrast. *Opt. Express* **2009**, *17*, 2518–2529.
6. Brehm, M.; Taubner, T.; Hillenbrand, R.; Keilmann, F. Infrared Spectroscopic Mapping of Single Nanoparticles and Viruses at Nanoscale Resolution. *Nano Lett.* **2006**, *6*, 1307–1310.
7. Stiegler, J. M.; Abate, Y.; Cvitkovic, A.; Romanyuk, Y. E.; Huber, A. J.; Leone, S. R.; Hillenbrand, R. Nanoscale Infrared Absorption Spectroscopy of Individual Nanoparticles Enabled by Scattering-Type Near-Field Microscopy. *ACS Nano* **2011**, *5*, 6494–6499.
8. Johnson, T. W.; Lapin, Z. J.; Beams, R.; Lindquist, N. C.; Rodrigo, S. G.; Novotny, L.; Oh, S.-H. Highly Reproducible Near-Field Optical Imaging with Sub-20-nm Resolution Based on Template-Stripped Gold Pyramids. *ACS Nano* **2012**, *6*, 9168–9174.
9. Huth, F.; Govyadinov, A.; Amarie, S.; Nuansing, W.; Keilmann, F.; Hillenbrand, R. Nano-FTIR Absorption Spectroscopy of Molecular Fingerprints at 20 nm Spatial Resolution. *Nano Lett.* **2012**, *12*, 3973–3978.
10. Amarie, S.; Zaslansky, P.; Kajihara, Y.; Griesshaber, E.; Schmahl, W. W.; Keilmann, F. Nano-FTIR Chemical Mapping of Minerals in Biological Materials. *Beilstein J. Nanotechnol.* **2012**, *3*, 312–323.
11. Amenabar, I.; Poly, S.; Nuansing, W.; Hubrich, E. H.; Govyadinov, A. A.; Huth, F.; Krutokhvostov, R.; Zhang, L.; Knez, M.; Heberle, J.; *et al.* Structural Analysis and Mapping of Individual Protein Complexes by Infrared Nanospectroscopy. *Nat. Commun.* **2013**, *4*, 2890.
12. Berweger, S.; Nguyen, D. M.; Muller, E. A.; Bechtel, H. A.; Perkins, T. T.; Raschke, M. B. Nano-chemical Infrared Imaging of Membrane Proteins in Lipid Bilayers. *J. Am. Chem. Soc.* **2013**, *135*, 18292–18295.
13. Huth, F.; Schnell, M.; Wittborn, J.; Ocelic, N.; Hillenbrand, R. Infrared-Spectroscopic Nanoimaging with a Thermal Source. *Nat. Mater.* **2011**, *10*, 352–356.
14. Amarie, S.; Keilmann, F. Broadband-Infrared Assessment of Phonon Resonance in Scattering-Type Near-Field Microscopy. *Phys. Rev. B* **2011**, *83*, 045404.
15. Zhang, L. M.; Andreev, G. O.; Fei, Z.; McLeod, A. S.; Dominguez, G.; Thiemens, M.; Castro-Neto, A. H.;

Basov, D. N.; Fogler, M. M. Near-Field Spectroscopy of Silicon Dioxide Thin Films. *Phys. Rev. B* **2012**, *85*, 075419.
16. Xu, X. G.; Rang, M.; Craig, I. M.; Raschke, M. B. Pushing the Sample-Size Limit of Infrared Vibrational Nanospectroscopy: From Monolayer toward Single Molecule Sensitivity. *J. Phys. Chem. Lett.* **2012**, *3*, 1836–1841.
17. Xu, X. G.; Tanur, A. E.; Walker, G. C. Phase Controlled Homodyne Infrared Near-Field Microscopy and Spectroscopy Reveal Inhomogeneity within and among Individual Boron Nitride Nanotubes. *J. Phys. Chem. A* **2013**, *117*, 3348–3354.
18. Hauer, B.; Engelhardt, A. P.; Taubner, T. Quasi-analytical Model for Scattering Infrared Near-Field Microscopy on Layered Systems. *Opt. Express* **2012**, *20*, 13173–13188.
19. Govyadinov, A. A.; Amenabar, I.; Huth, F.; Carney, P. S.; Hillenbrand, R. Quantitative Measurement of Local Infrared Absorption and Dielectric Function with Tip-Enhanced Near-Field Microscopy. *J. Phys. Chem. Lett.* **2013**, *4*, 1526–1531.
20. McLeod, A. S.; Kelly, P.; Goldam, M. D.; Gainsforth, Z.; Dominguez, G.; Thiemens, M.; Fogler, M. M.; Basov, D. N. The Lightning Rod Model: Quantitative Near-Field Spectroscopy for Extraction of Nano-resolved Optical Constants **2013**, arXiv:1308.1784.
21. Hillenbrand, R.; Keilmann, F.; Taubner, T. Scanning Method for Near Field Optical Microscopy Involves Illumination of Scanning Equipment Which Has Probe Litter with Lighting Equipment and Which Is Arranged in Predetermined Measuring Position above Surface of Sample; DE Patent App. DE200,510,029,823, 2006.
22. Taubner, T.; Keilmann, F.; Hillenbrand, R. Nanoscale-Resolved Subsurface Imaging by Scattering-Type Near-Field Optical Microscopy. *Opt. Express* **2005**, *13*, 8893–8899.
23. Krutokhvostov, R.; Govyadinov, A. A.; Stiegler, J. M.; Huth, F.; Chuvilin, A.; Carney, P. S.; Hillenbrand, R. Enhanced Resolution in Subsurface Near-Field Optical Microscopy. *Opt. Express* **2011**, *20*, 593–600.
24. Anderson, N.; Anger, P.; Hartschuh, A.; Novotny, L. Subsurface Raman Imaging with Nanoscale Resolution. *Nano Lett.* **2006**, *6*, 744–749.
25. Carminati, R.; Greffet, J.-J. Two-Dimensional Numerical Simulation of the Photon Scanning Tunneling Microscope. Concept of Transfer Function. *Opt. Commun.* **1995**, *116*, 316–321.
26. Carney, P. S.; Schotland, J. C. Inverse Scattering for Near-Field Microscopy. *Appl. Phys. Lett.* **2000**, *77*, 2798.
27. Carney, P. S.; Schotland, J. C. In *Inside Out: Inverse Problems and Appllications*; Uhlmann, G., Ed.; Cambridge University Press: Cambridge, 2003; Vol. 47; pp 133–168.
28. Sun, J.; Schotland, J. C.; Hillenbrand, R.; Carney, P. S. Nanoscale Optical Tomography Using Volume-Scanning Near-Field Microscopy. *Appl. Phys. Lett.* **2009**, *95*, 121108.
29. Carney, P. S.; Deutsch, B.; Govyadinov, A. A.; Hillenbrand, R. Phase in Nanooptics. *ACS Nano* **2012**, *6*, 8–12.
30. Garcia, N.; Nieto-Vesperinas, M. Near-Field Optics Inverse-Scattering Reconstruction of Reflective Surfaces. *Opt. Lett.* **1993**, *18*, 2090–2092.
31. Greffet, J.-J.; Carminati, R. Image Formation in Near-Field Optics. *Prog. Surf. Sci.* **1997**, *56*, 133–237.
32. Honigstein, D. R.; Weinroth, J.; Werman, M.; Lewis, A. Noniterative Exact Solution to the Phase Problem in Optical Imaging Implemented with Scanning Probe Microscopy. *ACS Nano* **2012**, *6*, 220–226.
33. Epstein, C. L.; Schotland, J. C. The Bad Truth about Laplace's Transform. *SIAM Rev.* **2008**, *50*, 504–520.
34. Hillenbrand, R.; Keilmann, F. Complex Optical Constants on a Subwavelength Scale. *Phys. Rev. Lett.* **2000**, *85*, 3029–3032.
35. Labardi, M.; Patane, S.; Allegrini, M. Artifact-Free Near-Field Optical Imaging by Apertureless Microscopy. *Appl. Phys. Lett.* **2000**, *77*, 621–623.
36. Taubner, T.; Keilmann, F.; Hillenbrand, R. Effect of Tip Modulation on Image Contrast in Scattering-Type Near-Field Optical Microscopy. *J. Korean Phys. Soc.* **2005**, *47*, 213–216.
37. Govyadinov, A. A.; Panasyuk, G. Y.; Schotland, J. C. Phaseless Three-Dimensional Optical Nanoimaging. *Phys. Rev. Lett.* **2009**, *103*, 213901.
38. Esslinger, M.; Vogelgesang, R. Reciprocity Theory of Apertureless Scanning Near-Field Optical Microscopy with Point-Dipole Probes. *ACS Nano* **2012**, *6*, 8173–8182.
39. Sun, J.; Carney, P. S.; Schotland, J. C. Strong Tip Effects in Near-Field Scanning Optical Tomography. *J. Appl. Phys.* **2007**, *102*, 103103.
40. Cvitkovic, A.; Ocelic, N.; Hillenbrand, R. Analytical Model for Quantitative Prediction of Material Contrasts in Scattering-Type Near-Field Optical Microscopy. *Opt. Express* **2007**, *15*, 8550–8565.
41. Aizpurua, J.; Taubner, T.; García de Abajo, F. J.; Brehm, M.; Hillenbrand, R. Substrate-Enhanced Infrared Near-Field Spectroscopy. *Opt. Express* **2008**, *16*, 1529–1545.
42. Ocelić, N. Quantitative Near-Field Phonon-Polariton Spectroscopy. Ph.D. Thesis, Technische Universität München, 2007.
43. Gaikovich, K. P.; Gaikovich, P. K.; Maksimovitch, Y. S.; Badeev, V. A. Pseudopulse Near-Field Subsurface Tomography. *Phys. Rev. Lett.* **2012**, *108*, 163902.
44. Greffet, J.-J.; Sentenac, A.; Carminati, R. Surface Profile Reconstruction Using Near-Field Data. *Opt. Commun.* **1995**, *116*, 20–24.
45. Bass, M.; DeCusatis, C.; Enoch, J.; Lakshminarayanan, V.; Li, G.; MacDonald, C.; Mahajan, V.; Van Stryland, E. *Handbook of Optics: Optical Properties of Materials, Nonlinear Optics, Quantum Optics*, 3rd ed.; Handbook of Optics; McGraw-Hill Education: New York, 2009; Vol. IV.
46. Malitson, I. H. Interspecimen Comparison of the Refractive Index of Fused Silica. *J. Opt. Soc. Am.* **1965**, *55*, 1205–1209.
47. Taubner, T.; Hillenbrand, R.; Keilmann, F. Nanoscale Polymer Recognition by Spectral Signature in Scattering Infrared Near-Field Microscopy. *Appl. Phys. Lett.* **2004**, *85*, 5064–5066.